An actively tunable terahertz metastructure absorber with tristate for refractive index sensing applications

Si-Ying Li, Hai-Feng Zhang [*]

College of Electronic and Optical Engineering & College of Flexible Electronics (Future Technology), Nanjing University of Posts and Telecommunications, Nanjing, 210023, China

ARTICLE INFO

ABSTRACT

Recently, the metastructure absorbers (MSA) have opened up a new sensing approach, whereas the existing designs suffer from a short numerical measurement range and small sensitivity span. In this paper, a photoexcited MSA that enables a transition between three operating states in the terahertz (THz) regime is proposed. The MSA merges two kinds of photosensitive semiconductor materials embedded in the split ring structure. By adjusting the wavelength of the pump light, semiconductor materials can be excited thus realizing the mutual change of three states in absorption. The structure appears to dual peaks absorption at normal incidence with absorptivity of 95.32% at 0.9269 THz and 99.42% at 1.5586 THz without the illumination of the pump light. Furthermore, it is worth emphasizing that we introduce a novel idea to utilize this actively tunable MSA for refractive index sensing. Not only it has the advantage of large sensitivity variation from 0.0471 (THz/RIU) to 0.1239 (THz/RIU) but also it can be applied in five different refractive index numerical measurement ranges spanning from 1 to 4 with preferable performance. Finally, the absorption effect of the MSA is analyzed under different incidence and polarization angles.

1. Introduction

The terahertz (THz) spectrum commonly refers to electromagnetic waves between 0.1 and 10 THz. Because of the low photon energy, strong penetration, and good directivity of THz radiation, THz technology has been widely used in applications such as imaging, medical diagnosis, security detection, environmental monitoring, high-speed broadband, and so on [1–6]. THz has attracted widespread attention due to the rich physical and chemical information in THz spectroscopy, which has unique advantages in analyzing the morphology and structural components of substances. Although THz waves exist widely in nature, most materials in nature have weak electromagnetic responses in the THz frequency band. The emergence of THz metamaterials has brought new opportunities for the development and application of THz science and technology.

Metamaterials have attracted huge attention in terms of their exotic properties. With unit cells on the sub-wavelength scale, such characteristics can be realized like invisibility cloaking, perfect lens, and negative refractive index [7–10]. Such a subwavelength periodic structure processes eminent adaptability from microwave to THz and optical frequencies. Now metamaterials have been widely used in

various electromagnetic devices, such as distributed amplifiers, broadband phase shifters, sensors [11,12], and absorbers [13–15]. Landy et al. design the first perfect metamaterial absorber, which is made up of a metallic split ring and a cut wire separated by a dielectric layer [16]. However, the excellent electromagnetic properties possessed by metamaterials are mainly determined by the shapes and physical sizes of artificially designed structural units, which limits their electromagnetic properties. It has been found that metamaterials with dynamically tunable electromagnetic properties can be used for certain specific frequencies and are well-developed for many applications such as sensing, frequency selection, and narrowband filtering [17].

Nowadays, a massive effort has been devoted to the research of dynamic control of the absorption frequency and intensity of metamaterial absorbers. The switchable/tunable absorbers have aroused intense attention by virtue of flexibility and fabricability in practical application scenarios [18–24,27–30]. Under the condition that the structural parameters remain unchanged, conventional absorbers hardly achieve the absorption mode of the frequency change, which is considered inconvenient [31]. In terms of the shortcomings, switchable/tunable absorbers are definitely superb options with plenty of methods such as thermal control [20–22], electrical control [23,24], and optical control

---

[27–30] are highly feasible. When it comes to these methods, semiconductor materials as well as some phase-change materials, like vanadium dioxide, have become fabulous choices [19–24,27–33]. The conductivity of these materials can be adjusted by temperature, bias voltage, or optical power, thus one can regulate the resonance characteristics after merging these materials into the absorbers. Liquid crystals are also awesome candidates for tunable and dynamic metamaterials with many untapped potentials [25,26]. Besides, Baranzadeh, F et al. used liquid crystal in the proposed structure to tune the structure by variation of the incident angle and applying the external bias field to obtain the near-perfect and ultra-narrow absorption peak [27].

The absorbers used in the two-dimensional plane structure mentioned above are known as metasurfaces, which are exactly a branch as well as a subset of metastructures. Metastructures whose applications are virtually the same as metasurfaces are offshoots and 3D extensions of metasurfaces [28]. With the soaring number of multilayer structures caused by the escalation of application requirements, the conventional metasurfaces which are used to define 2D systems are no longer suitable for defining 3D cases [29]. Consequently, numerous tunable MSAs emerge as the times require. What's more, MSAs are suitable for sensing because the resonance frequencies of metamaterial structures are very sensitive to variations caused by capacitive and inductive effects. A case in point is that the narrow-band MSAs, which are based on metamaterials, are capable of marvelous refractive index sensing performance. The refractive index sensors with good characteristics of fast detection speed and low pollution have been extensively used in the biological sensing [37–40]. However, attention should be deserved as achieving a multi-band MSA with high-sensitivity sensing is still a thorny problem.

In the study, a photoexcited tristate tunable MSA is designed to realize multi-band absorption as well as refractive index sensing [41]. The MSA is mainly composed of metal split rings, a dielectric interlayer, a gold backplane, and two kinds of photosensitive materials. By tuning the conductivity of the photosensitive semiconductor germanium (Ge) and silicon (Si), the MSA can achieve the mutual change of the three states in absorption when semiconductors Ge and Si are excited or not by different wavelengths of the pump light [41]. Without the illumination of the pump light, the MSA exhibits two peaks with absorptivity of 95.32% at 0.9269 THz and 99.42% at 1.5586 THz. Upon only Ge being excited, peaks appear with absorptivity of about 99.38% at 0.7790 THz and 99.37% at 1.9506 THz. When Ge and Si are both motivated by adjusting the pump light, the equipment displays absorption peaks with the absorption of 99.21% and 99.10% at 0.7490 THz and 1.8537 THz.

Clearly, our designed structure can form 5 perfect absorption points in three different states. Meanwhile, thanks to the axial symmetry of the MSA, it is polarization insensitive to transverse electric (TE) and transverse magnetic (TM) polarization. The impedance matching theory is employed to understand the physical mechanism of the designed MSA. Furthermore, the absorption effect of the given MSA in different polarizations and incidence angles is also analyzed in detail. At the same time, we have found that MSA has good refractive index sensing properties for detecting the surroundings. The simulation results show that the sensor not only can measure a wide refractive index range from 1 to 4 but also has the advantage of a large difference in sensitivity under the condition of three different states. That says it can better meet the needs of measuring different media with the functions of multi-band tunable absorption as well as refractive index sensing. We are convinced that this proposal can offer potential applications in various biomedical, environmental monitoring, and medical diagnostics.
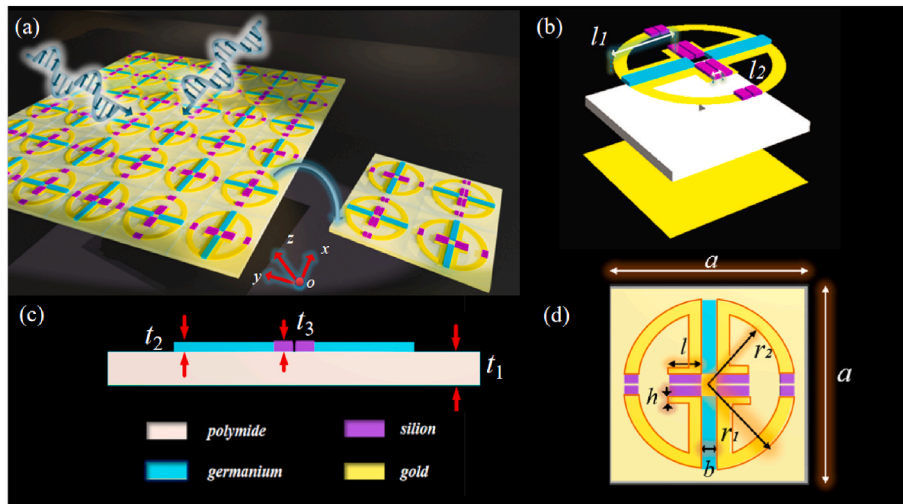
2. Structure design

The ultimate periodic principle and the final structure of the configuration are elaborated in Fig. 1(a). Rotating the unit cell along the *z*-axis is a fabulous option in terms of improving polarization characteristics. The unit can be divided into three layers for further narration as shown in Fig. 1(b), where Ge and Si are placed around a top metal resonator consisting of the first layer. The top metal rings are gold with a conductivity of $\sigma = 4.561 \times 10^7$ S/m [30]. What is composed of the second element is a dielectric spacer, which is made of polyimide with a relative dielectric constant of $\varepsilon = 3.5$ and a loss tangent of $\tan \delta = 0.003$ [44]. A gold backplane with a thickness of 0.2 μm is regarded as the third component.

As depicted in Fig. 1(d), two *y*-oriented Ge wires and four Si blocks are embedded at the intersection of the top metal resonator made of four-quarter rings, which resembles the shape of an ancient Chinese copper coin. In a bid to display the structure explicitly, the side view is

Table 1
Geometric parameters for the demonstrated equipment.

Parameter	Value (μm)	Parameter	Value (μm)	Parameter	Value (μm)
a	105	l	17	t_2	2.4
b	8	l_1	39	t_3	2
r_1	45	l_2	5.5	h	4
r_2	38	t_1	7.3		

Fig. 1. Schematics for the proposed MSA with the periodic arrangement and unit cell. (a) The periodic topological arrangement of the MSA with the unit cell extracted at the bottom right. (b) The triple-layers sectional view for the model. (c) Side view of the structural units. (d) Front view of the structural units.

manifested in Fig. 1(c) as well as optimized geometrical parameters are integrated into Table .1.

For simplicity, we use σ_1 to refer to the conductivity of Ge and σ_2 to refer to the conductivity of Si. Due to the diverse applied wavelengths of pump light, Ge and Si have different conductivities. Therefore, an adjustable MSA can be realized by whether Ge and Si are excited or not. It is noteworthy that the left and right quarter rings can be connected via Ge and the Si influences the gap between the upper and lower quarter rings. Such delighting phenomenon verifies the sensing application. And the analyte, whose thickness is 3 μm, is laid in the position shown in Fig. 2 with the front elevation of the construction without it.

To verify the efficiency of our design, the software High Frequency Structure Simulator (HFSS) is employed to obtain the electromagnetic response of the proposed MSA. The Master-Slave boundary conditions are set to calculate this infinite periodic unit and the Floquet port setting upon this MSA is used to the simulation that the electromagnetic waves (EM) along the -*z*-direction is vertically incident on the target matter from infinity while the periodic boundary conditions in the *x*-axis and *y*-axis are employed for the transverse boundaries to replicate an infinite array of the MSA. In this analog, the TE wave is assumed that the electric field is parallel to the *y*-axis while the magnetic field is parallel to the *x*-axis, which is in contrast to the TM wave in which the electric field is parallel to the *x*-axis and the magnetic field is parallel to the *y*-axis.

The absorbers are typically characterized by a nontrivial indicator absorption $A(\omega)$. The absorption $A(\omega)$ can be numerically acquired by

$$A(\omega) = 1 - R(\omega) - T(\omega) - P(\omega) \tag{1}$$

where $R(\omega) = |S_{11}|^2$ denotes reflectance, $T(\omega) = |S_{21}|^2$ represents transmittance, and $P(\omega)$ indicates the conversion of polarization. When the THz wave is a normal incidence of a given MSA, no transmission can be examined as the thickness of the gold film is enough to meet the typical skin depth of EM [44]. Thus, the transmittance of the MSA is zero ($T(\omega) = 0$). Besides, such a designed device is highly symmetrical, therefore the polarization states of the MSA have an extremely slight effect on the absorption curve, which means that the absorbance can be described as $A(\omega) = 1 - R(\omega)$ [45–48].

3. Results and discussion

Compared with Si, Ge can be motivated by pump light with a wavelength less than 1800 nm since Ge has lower bandgap energy at room temperature 300 K, while Si can be motivated when the wavelength of the pump light is less than 1100 nm [42,43]. With peaked pump beam power, the conductivities of Ge and Si are considered as 0 S/m for no pump beam lighting and are gradually increased to 1×10^6 S/m. Additionally, the change in the conductivity of Si is consistent with that of Ge in the condition that Si and Ge are both motivated [41,48–53].
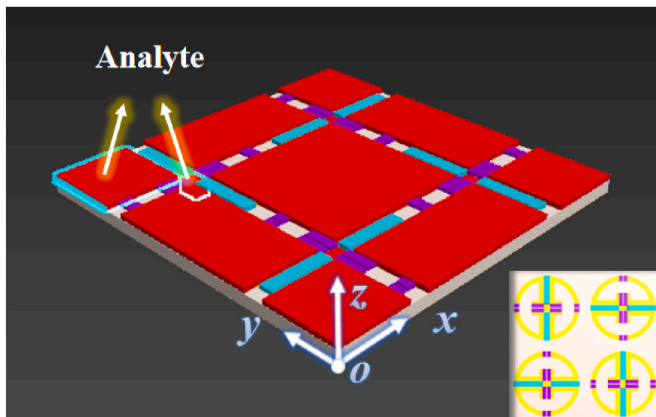

Fig. 2. Front elevation of the construction and the position of the analyte.

Some properties above are consistent with the fitting experimental results in Ref. [52].

As delineated schematically in Fig. 3, when no pump light incidence, the MSA has two absorption peaks with absorptivity of 95.32% at 0.9269 THz and 99.42% at 1.5586 THz. With 1550 nm pump light applied, only Ge wires are motivated by the pump light intensity and Ge exhibits metallic properties [42]. Peaks are formed at 0.7790 THz and 1.9506 THz with absorptions of 99.38% and 99.37% when σ_1 is 1×10^6 S/m. When applying 800 nm pump light, both Ge and Si are motivated, presuming that the change in conductivity of Ge and Si is consistent, a double-band absorption appears with absorptivity of 99.21% and 99.10% at 0.7490 THz and 1.8537 THz when $\sigma_1 = \sigma_2 = 1 \times 10^6$ S/m.

And this dynamic adjustability is exactly what refractive index sensing required. Fig. 4 exhibits the absorptivity of the MSA when σ_1 and σ_2 vary while the refractive index (n) of the analyte remains 1. It can be seen that the curves in Figs. 3 and 4 are not the same as the n of air is not 1, so the situation where there is no analyte and the n of the analyte is 1 will be different. To more clearly illustrate the transition, state 1 is introduced when neither Ge nor Si is excited ($\sigma_1 = \sigma_2 = 0$ S/m). When Ge is motivated but Si is not ($\sigma_1 = 1 \times 10^6$ S/m, $\sigma_2 = 0$ S/m), it is represented by state 2. When both Ge and Si are stimulated ($\sigma_1 = \sigma_2 = 1 \times 10^6$ S/m), state 3 is applied.

As elucidated in Fig. 4, when no external illumination ($\sigma_1 = \sigma_2 = 0$ S/m), symmetrical quarter rings independently respond to the incident EM wave, exhibiting dual-band absorption at 0.9305 THz and 1.5365 THz in TE mode. As the pump beam power starts to enhance, the conductivity of Ge and Si increases gradually, giving rise to the changes in the peak points. The MSA achieves two peak points at 0.7760 THz and 1.7810 THz when Ge acts alone. Noted that the absorption is almost perfect at 1.7810 THz with an absorptivity of 99.97%. What's more, the MSA forms three absorption peaks at 0.7460 THz, 1.1858 THz, and 1.7432 THz when Ge and Si serve together. The absorption rates are 98.84%, 90.29%, and 97.71%, from which we can see apparently that all are above 90%, indicating preferable properties.

To elucidate the physical principle of the phenomenon that the absorption is satisfactory, the surface current distributions in the *x-y* plane at the first absorption peak point of the three states are elaborated intuitively in Fig. 5 and Fig. 6, in which the direction of the current flow is marked by the red dashed line and the color represents the intensity.

As we know, surface current distribution can be different when the EM enters two wires. Supposing that the two wires maintain an anti-parallel current, magnetic resonance can be formed. Similarly, the electrical resonance can be obtained when the two wires have parallel currents. Hence, we can explain the physical mechanism of the proposed configuration by observing the surface current distributions of the resonator as well as the bottom metal plate. The TE mode is taken as an example in the following representation for the formation principle of the MSA is identical to the TE and TM modes. Referring to Fig. 5(a) and (b), the strong resonant occurred to the upper left and lower right of the structure at 0.9330 THz in state 1, which indicates that the impedance matching principle is fulfilled by the setting of the materials, along with the loss of energy attributed to the high loss tangent of the polyimide. We can find that the distributions of surface current are sensitive to the polarization states of incident waves. However, the commonality of the two modes is that the rings parallel to the electric field excite the current. Apart from that, the thick metal ground can virtualize the real current inspired inside the metal rings, thus markedly strengthening the intensity of confined fields, meanwhile, much electromagnetic power within the MSA can be absorbed. Hence the absorption of the MSA will also be more desirable.

When the incident light with the electric field is reflected and transmitted at the analyte-spacer interface with the MSA, it can induce the regular movement of electrons within the metal resonance cell and generate displacement currents. Two sets of anti-parallel currents are formed at the top resonator along the *x*-axis. And two sets of parallel currents are generated at the upper and lower parts of the top resonator
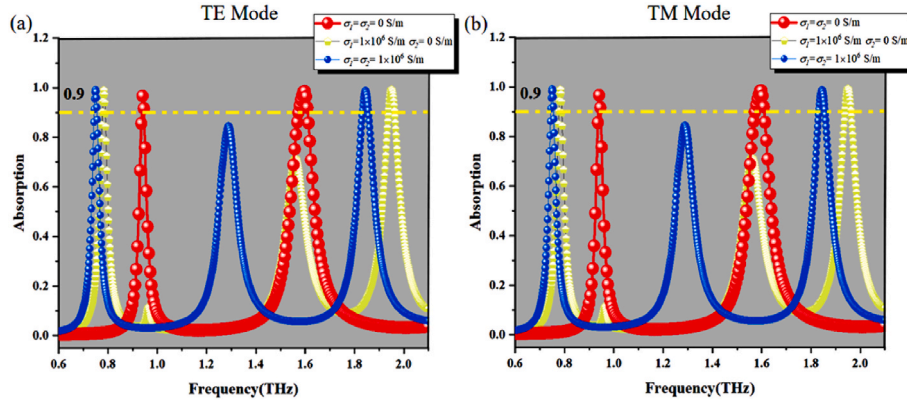
Fig. 3. The absorptivity of the MSA without analyte when σ_1 and σ_2 change with the wavelength of the pump light, (a) in the TE mode, (b) in the TM mode.
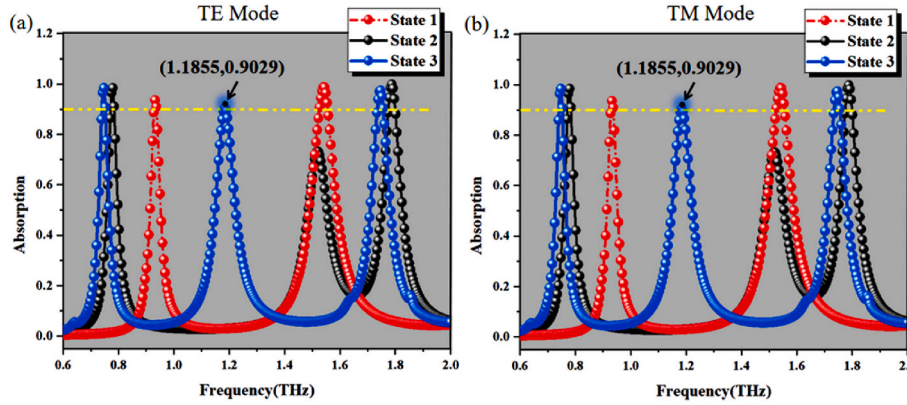

Fig. 4. The absorptivity of the MSA for three states ($n = 1$), (a) in the TE mode, (b) in the TM mode.

along the y-axis. Based on the aforementioned analysis, it can be inferred that electrical and magnetic resonances are induced at quarter rings. At the same time, anti-parallel currents and closed loops are inspired by the metal bottom plate and the top metal rings, which play relatively high magnetic resonance. On balance, the absorption can achieve the maximum value of 95.04% at 0.9330 THz owing to electrical and magnetic resonances. We also explore the surface current distribution of the high-frequency resonance point of the structure in state 1. As shown in Fig. 5(c) and (d), anti-parallel currents and closed loops are formed by the bottom plate and metal rings at 1.537 THz.

As manifested in Fig. 5(e), two circular parallel currents along the loop in state 2, which can couple the electric field component of the incident THz wave, can induce electric dipoles and result in electric resonance responses. We have known that the dielectric constant and the thickness of the dielectric layer significantly affect the coupling between two metallic layers, which results in magnetic resonance. It can be concluded from Fig. 5(e) and (f) that the top resonator responds to the magnetic field component of the incident THz wave. Anti-parallel currents and closed current loops with the gold backplane are aroused, which shows an excitation of magnetic response and gives rise to consume the energy of the incident EM. It is worth noting that the MSA exhibits perfect absorption performance at 0.7660 THz with an absorptivity of 98.80% owing to electric resonance and magnetic resonance. As displayed in Fig. 5(g) and (h), currents in the opposite directions are formed near the rings and the absorption principle of the high-frequency absorption point at 1.763 THz, which will not be repeated again. Meanwhile, the surface current distribution for state 3 is almost identical to that of state 2 as depicted in Fig. 5(i)–(l). Similar to state 2, we can deduce that the appearance of the absorption peaks at 0.7115 THz and 1.678 THz are related to electrical and magnetic resonances.

The distributions of the absolute value of the surface current for the three states are shown in Fig. 6. It is found that the currents are mainly distributed on the metal rings, where energy dissipation is concentrated. To be precise, the currents are mostly distributed around the annular gaps and on both sides of the Ge wires in state 1 as illustrated in Fig. 6(a). In state 2 and state 3, the currents are mainly concentrated in the annular gaps and their surrounding area, just like what Fig. 6(b) and (c) display. By analyzing Fig. 6 comprehensively, we can deduce that when Ge is not excited, a capacitor is formed where it is. That says currents are accumulated around Ge wires. However, Ge shows metallic properties when it is motivated, with the result of connecting the metal rings on both sides. Hence, the currents will gather elsewhere in the rings instead of near the Ge wires. The effect of Si is similar as it influences the width of the gaps between the rings when it acts. Nevertheless, limited by its size, it will not link the upper and lower rings. Additionally, the rings along the diagonal line from the lower left to the upper right corner are excited in stark contrast to the situation of the TM mode, where the rings at the upper left corner and the lower right corner of the structure appear the excitation.

Leveraging the depiction and analysis of the corresponding distributions of the electric field in the proposed structure, the mechanism of the absorption mentioned formerly can be verified. As observed in the corresponding distributions of the electric field from Fig. 7(a), the energy of fields can be strongly localized around Ge and rings at 0.9330 THz in state 1. When it comes to states 2 and 3, the energy of fields is mainly distributed at the gaps and the surrounding area of the rings as shown in Fig. 7(b) and (c). The description of the above series of simulation results, which gives strong testimony to confirm the analysis with respect to the formation of absorption peaks, proves the optimized
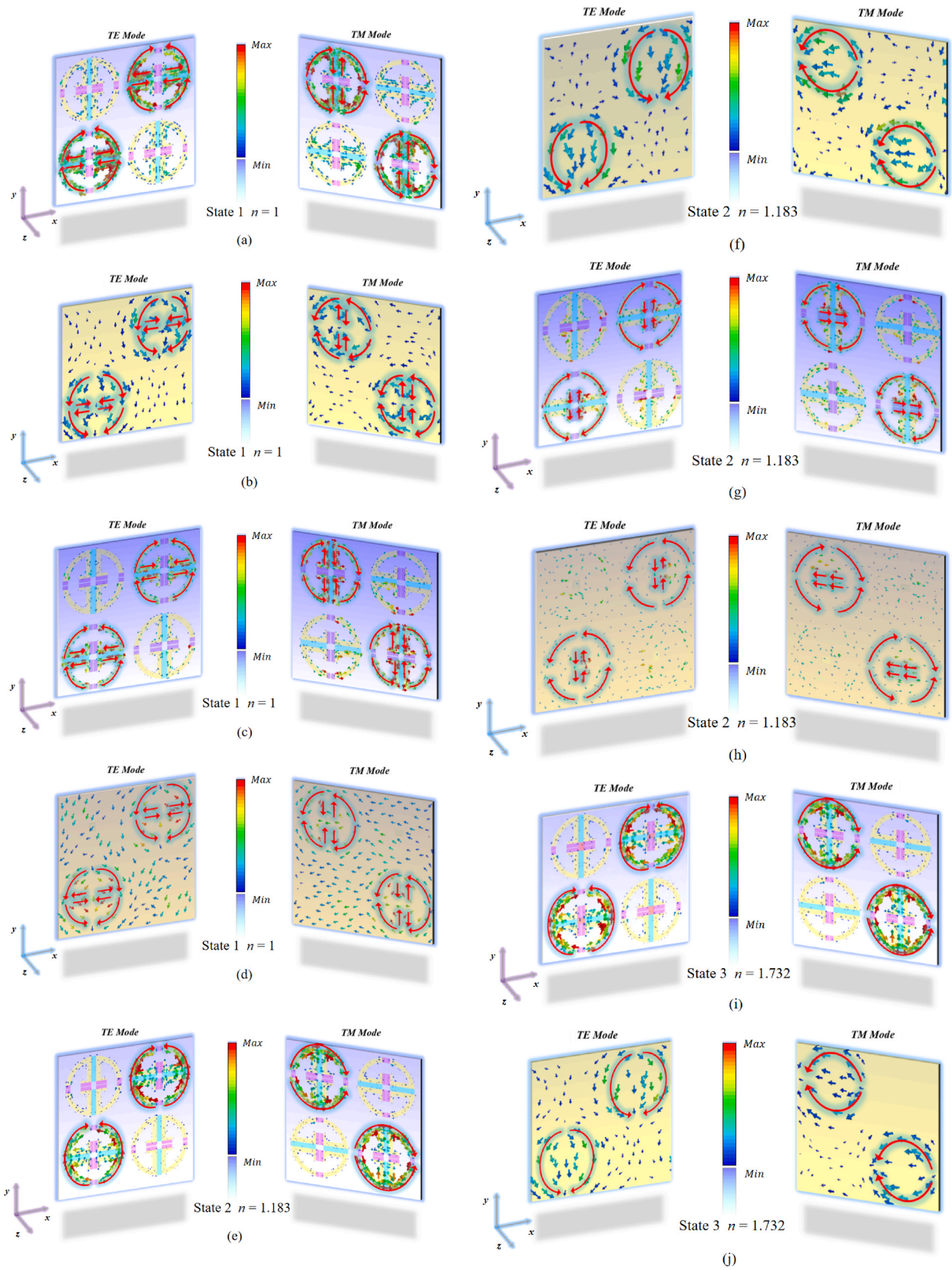
Fig. 5. Surface current distributions of the MSA surface: (a) at 0.9330 THz in state 1 ($n = 1$). (c) at 1.537 THz in state 1 ($n = 1$). (e) at 0.7660 THz in state 2 ($n = 1.183$). (g) at 1.763 THz in state 2 ($n = 1.183$). (i) at 0.7115 THz in state 3 ($n = 1.732$). (k) at 1.678 THz in state 3 ($n = 1.732$). Surface current distributions of the gold plate: (b) at 0.9330 THz in state 1 ($n = 1$). (d) at 1.537 THz in state 1 ($n = 1$). (f) at 0.7660 THz in state 2 ($n = 1.183$). (h) at 1.763 THz in state 2 ($n = 1.183$). (j) at 0.7115 THz in state 3 ($n = 1.732$). (l) at 1.678 THz in state 3 ($n = 1.732$).
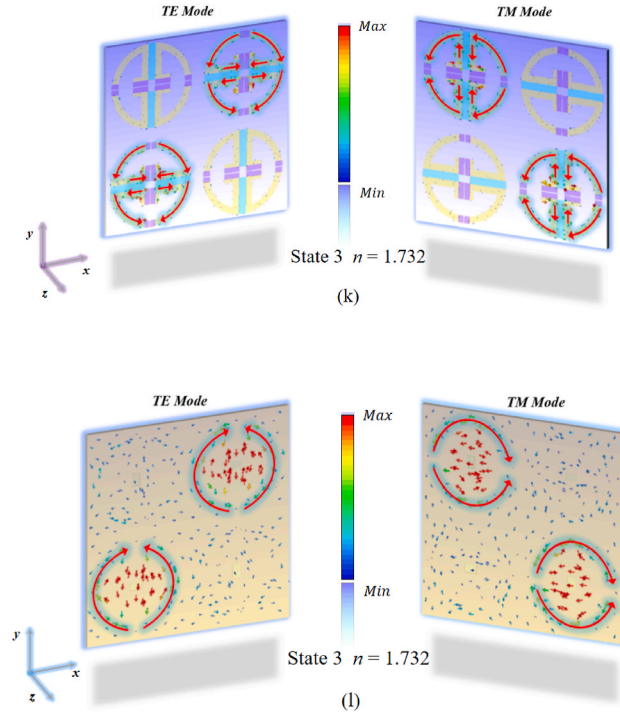
Fig. 5. (*continued*).

model's feasibility in theory.

To further prove that impedance matching is indeed achieved and the rationality of the designed structure, we simulated and calculated the impedance z, while the relationship between the impedance z and the S-parameter is:

$$z = \pm \sqrt{\frac{(1 + S_{11})^2 - S_{21}^2}{(1 - S_{11})^2 - S_{21}^2}} \tag{2}$$

The corresponding S-parameters can be obtained from the transmission matrix T [54], in which d means the thickness of the MSA, $k = \omega/c$ represents the transmitted wave number, $n = n_1 + in_2$ and $z = z_1 + iz_2$ refer to the refractive index and impedance respectively.

$$T = \begin{pmatrix} \cos(nkd) & -\frac{z}{k}\sin(nkd) \\ \frac{k}{z}\sin(nkd) & \cos(nkd) \end{pmatrix} \tag{3}$$

$$S_{11} = \frac{i}{2}\left(\frac{1}{z} - z\right)\sin(nkd) \tag{4}$$

$$S_{21} = \frac{1}{\cos(nkd) - \frac{i}{2}\left(\frac{1}{z} + z\right)\sin(nkd)} \tag{5}$$

As mentioned above, $R(\omega) = |S_{11}|^2$ and $T(\omega) = |S_{21}|^2$. When the impedance is matched perfectly ($z = 1$) as well as n_2 tends to the infinity, $R(\omega) = T(\omega) = 0$. That says the absorption reaches the maximum. Owing to the gold backplane, S_{21} is zero.

Due to the symmetrical characteristics of the design, it is only necessary to talk about the impedance z of the MSA in TE waves, and the simulation results calculated by Eq. (2) are described in Fig. 8, where the red and blue curves correspond to the real part and the imaginary part. It can be clearly observed in Fig. 8(b) that near the two absorption peaks, the real part of the impedance z (Re) approximates 1, and the imaginary part (Im) is close to 0, respectively, which means that the structure can extraordinarily match the impedance of free space when EM waves are incident vertically so that more EM waves can enter into the equipment

and be lost without being reflected. What is deserved to say is that at 0.9330 THz, Re = 1.0293, Im = 0.0060, attributing to the perfect absorptivity of 95.04%. Fig. 8(a) provides strong evidence for the above views and r_{xx} and r_{yx} are the co-polarized reflection coefficient and the cross-polarized reflection coefficient separately. Black elements represent r_{xx} while red elements refer to r_{yx}. With the aim of better stating the problem, the peak points of r_{xx} have been marked. What can be seen vividly is that the amplitude of r_{xx} decreases rapidly at 0.9330 THz and 1.5365 THz, while the amplitude of r_{yx} remains stable at less than 0.05. This demonstrates that the MSA offers an efficient absorption effect in the two peaks. When it comes to the other two states, the situations of the impedance z are similar to state 1 as shown in Fig. 8(d) and (f), indicating that effective impedance matching occurs between the MSA and free space, and will not be repeated here for the sake of preventing the repetition of content. Moreover, both r_{xx} and r_{xy} are very small in Fig. 8(c), illustrating that the absorption rate will be desirable, which is consistent with the previous absorption curves and proves the rationality of the MSA. In comparison, the r_{xx} of Fig. 8(a) and (e) are relatively high, but they are in the acceptable scope with values less than 0.2. To sum up, our designed structure is pretty convincing in physical principles.

And Fig. 9(a) displays the dynamically switchable absorption of the devised resonator when σ_1 changes while σ_2 is zero. We find that as σ_1 increases, the absorption points shift in the direction of the longer wavelengths. When σ_1 reaches 8×10^3, the second absorption point begins to split into two absorption points. The difference between the two split absorption points gradually becomes obvious as the σ_1 increases. When the MSA is in state 3, the changes of σ_1 and σ_2 are consistent. From Fig. 9(b), it can be found that with the increase of σ_1 and σ_2, the absorption values of the two absorption peaks gradually decrease, and then three absorption peaks are formed.

By further exploring the tunability of the MSA, we find that the resonance wavelengths of the sensor have an approximately linear correlation with the refractive index of the materials under sensing. We extracted the shifts of absorption peaks under different states and different n. As shown in Fig. 10(a), the absorption peak shifts linearly as n varies from 1 to 1.2649 when in state 1. Besides, with the increase of n,
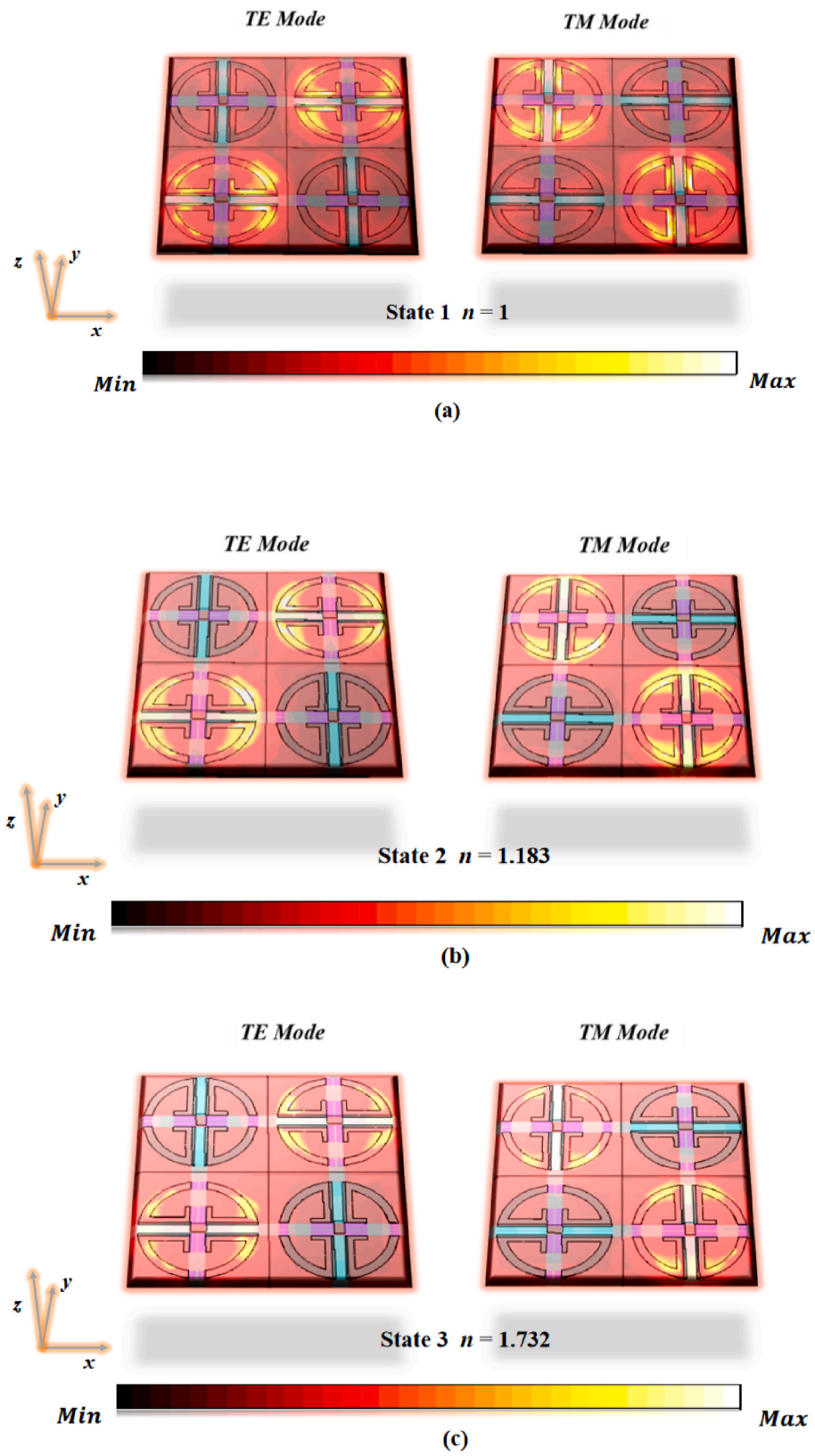
Fig. 6. The distribution of the absolute value of the surface current: (a) at 0.9330 THz (state 1, $n = 1$) (b) at 0.7660 THz (state 2, $n = 1.183$) (c) at 0.7115 THz (state 3, $n = 1.732$).

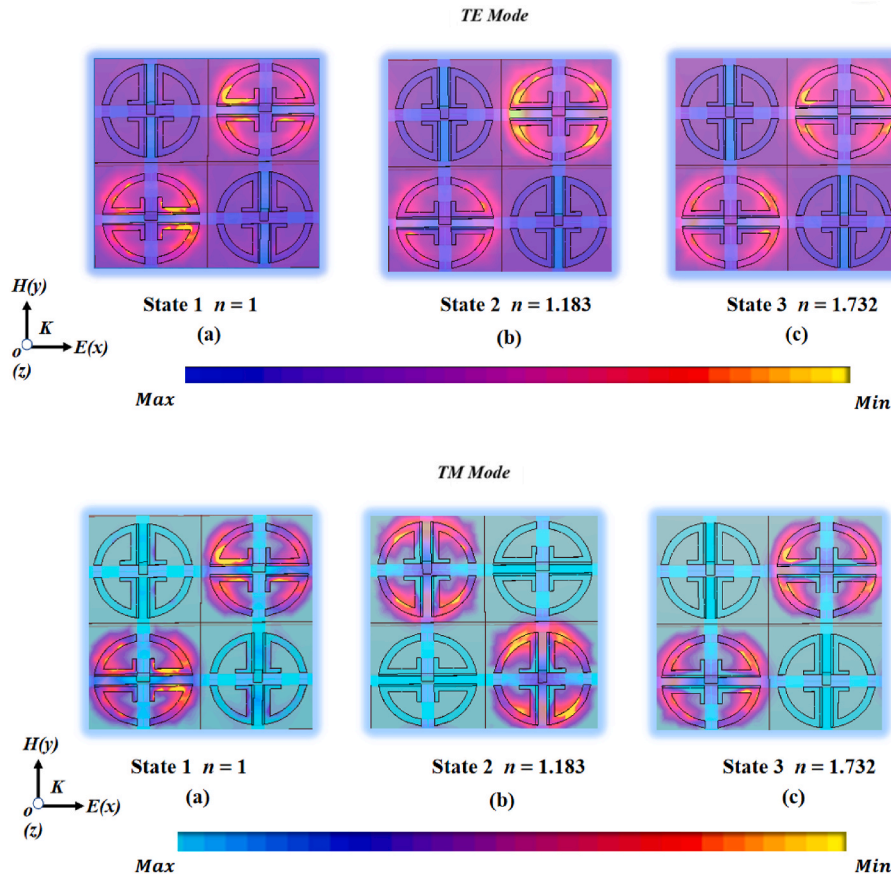**Fig. 7.** The distribution of the absolute value of the electric field: (a) at 0.9330 THz (state 1, $n = 1$) (b) at 0.7660 THz (state 2, $n = 1.183$) (c) at 0.7115 THz (state 3, $n = 1.732$).

the absorption curves show a clear red shift phenomenon. This is due to the obvious change in the dielectric constant of the analyte, which is reflected in the change of the resonance frequency by the sensor. What's more, the other two states also exhibit this property. Apart from that, the absorption effect is so fabulous with the absorptivity exceeding 98% in both state 2 and state 3, which is clearly displayed in Fig. 10(b) and (c). The sensitive change of the resonance frequency with the external n is a significant characteristic and essential condition of the sensor for refractive index sensing applications. To this end, we conduct an in-depth study about the structure we proposed and the research findings are illustrated below.

Based on the above-mentioned phenomenon of linear change, five different measuring ranges are found. As illustrated in Fig. 12, when the sensor functions in state 1, the measurable range of n has two parts, which are 1–1.2649 and 1.7321–2.6458. The measurement of n is 1.1464–2 and 2–4 when it is in state 2 whereas its measurement of n is 1–2.2361 in the case of state 3. After the simulation calculation, we get that in state 1, when the n is in the range of 1–1.2649, the sensitivities of the two resonance points of the structure are 23.55 and 22.4. As the n range is 1.7320–2.6458, the sensitivities of the two resonance points are 63.4 and 60.8, thus the first resonance point is selected for sensor measurement. Similarly, in state 2, when the n is 1.1464–2, the sensitivities of the three resonance points are 24.5, 32.1 and 109.8. Therefore, the third resonance point is chosen. For the case of state 3, the sensitivities of the three resonance points are 20,14.9 and 47.1, respectively. Take the first numerical measurement range of state 1 as an instance. By taking points linearly, the linear fitting equation is expressed as $f = -0.0552n + 0.9876$, which means that the sensitivity (S) is about 0.0552 (THz/RIU). R-square plays a significant role in describing the linearity, which is superior since R-square is as high as

0.99886. The linear fitting curves in all measuring ranges are displayed in Fig. 11, reflecting good linear characteristics.

The refractive index distribution of many substances is in the range of 1.3–1.8, which is included in the measuring range of the sensor. Its excellent properties allow it to be extended in a variety of applications such as the detection of biological tissue, pesticide residues in food, etc. S and figure of merit (FOM) and quality factor (Q) are important parameters for measuring refractive index sensors [52,53]. The S of the refractive index sensor is specified as $S = \Delta f/\Delta n$, where Δf and Δn are the variation of the resonant frequency point and the change in the surrounding refractive index [56]. And the FOM can be expressed as FOM = S/FWHM, in which FWHM is the full width at half maximum. Q = f_T/FWHM, while f_T symbolizes resonant frequency. Via simulating the MSA, deriving and calculating the numerical results, we get specific information displayed in Fig. 12 in which Q and FOM take the maximum value in the range. What is distinctly depicted is that the highest S of the three states can reach 0.0634 THz/RIU, 0.1239 THz/RIU, and 0.0471 THz/RIU whereas corresponding FOM can be 1.696, 2.380, and 1.195. The maximum Q value of the sensor is 23.55, and the higher quality factor Q indicates that the designed sensor has higher frequency selection characteristics.

Moreover, it is noteworthy that the values of S and FOM in different numerical measurement ranges of the same state are also very different. Distinct from most previous sensors, the MSA we proposed has a wide numerical measurement range and far different S in diverse states, which can meet the needs of disparate precisions for measuring substances and be applied on many occasions. In contrast, the S of the sensor made by Shen et al. remains almost unchanged, which limits the sensor's many applications [57]. Besides, the absorption peaks in the three states of our MSA are relatively high, whereas the structure designed by Yi
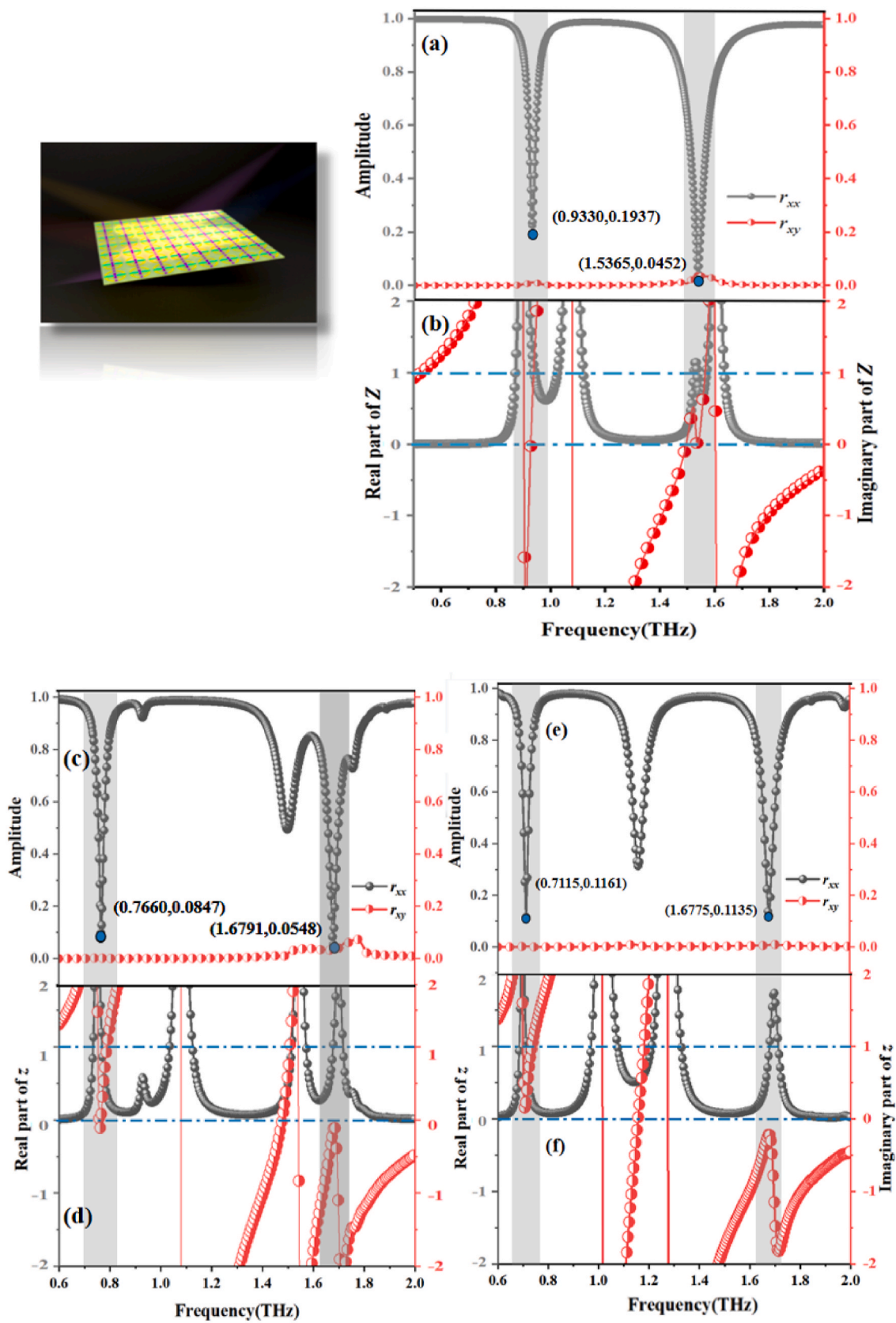
Fig. 8. The reflection amplitude curves. (a) state 1 $n = 1$. (c) state 2 $n = 1.183$. (e) state 3 $n = 1.732$. The normalized complex impedance *z* of the proposed MSA. (b) state 1 $n = 1$. (d) state 2 $n = 1.183$. (f) state 3 $n = 1.732$.
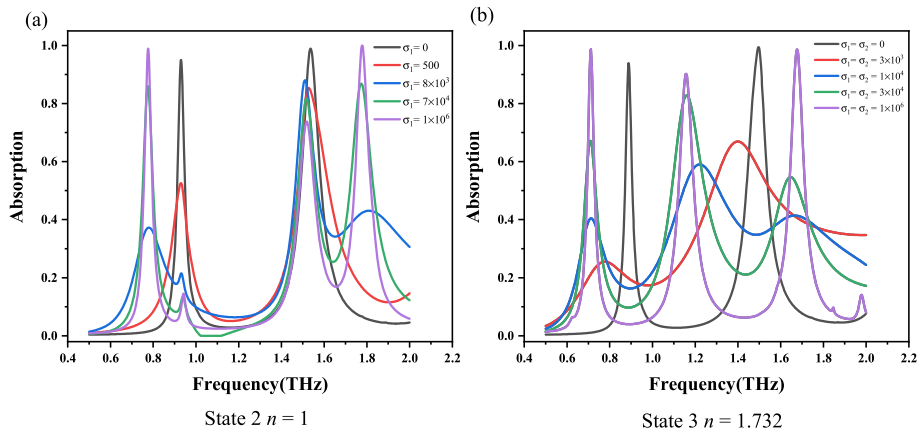
Fig. 9. (a) The curves of the absorption in state 2 when σ_1 varies. (b) The curves of the absorption in state 3 when σ_1 and σ_2 change in the same way.
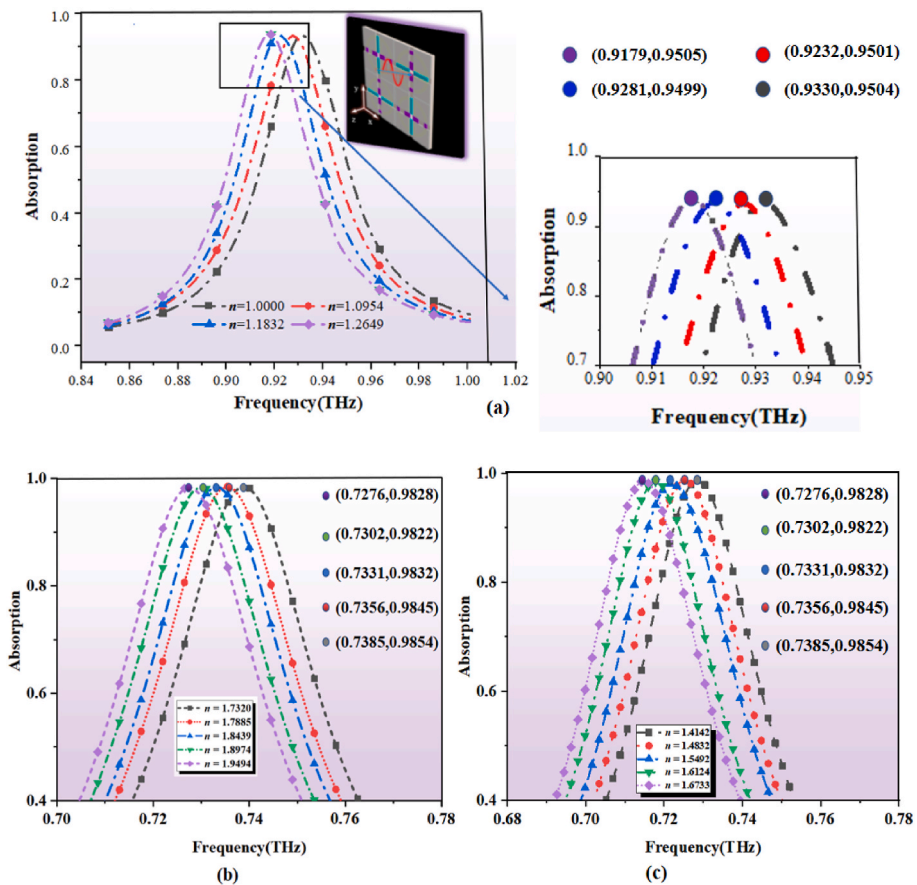

Fig. 10. (a) The absorptivity of the absorber when n changes from 1 to 1.2649 in state 1. (b) The absorptivity of the absorber when n changes from 1.7320 to 1.9494 in state 2. (c) The absorptivity of the absorber when n changes from 1.4142 to 1.6753 in state 3.

et al. has a peak of 65.7% [58]. The comparison between the sensor we designed and the previous sensors is exhibited in Table .2. All in all, the proposed sensing structure proved to be capable of multi-band sensing function, on one hand, tunability of the S and FOM within a certain range, on the other hand, which complies with the trend of multiple application scenarios of sensors and furnishes an essential reference to the THz sensor design.

All the above discussions are under normal incidence. To meet the requirements of the validation work as well as show the device's adaptability to complex environments to some extent, it is necessary to analyze the absorption effects under different incidence angles (θ). We

investigate the angular stability of the structure and the absorption spectra under different θ and states are depicted as shown in Fig. 13. It can be seen in Fig. 13(a) that for TE mode when the θ is increased from 0° to 75° with a span of 15°, the absorptivity of the two peaks is gradually reduced. Especially when the θ is 75°, both absorption peaks drop significantly. To summarize, it maintains good absorption performance with θ less than 45° when in state 1. Similarly, as the θ continues escalating, the absorption performances suffer a dramatic decline of around 1.7 THz in state 2 as shown in Fig. 13(b). This phenomenon can be attributed to the fact that with the θ increasing, the electric field components of the EM arrive at different resonant structures at diverse
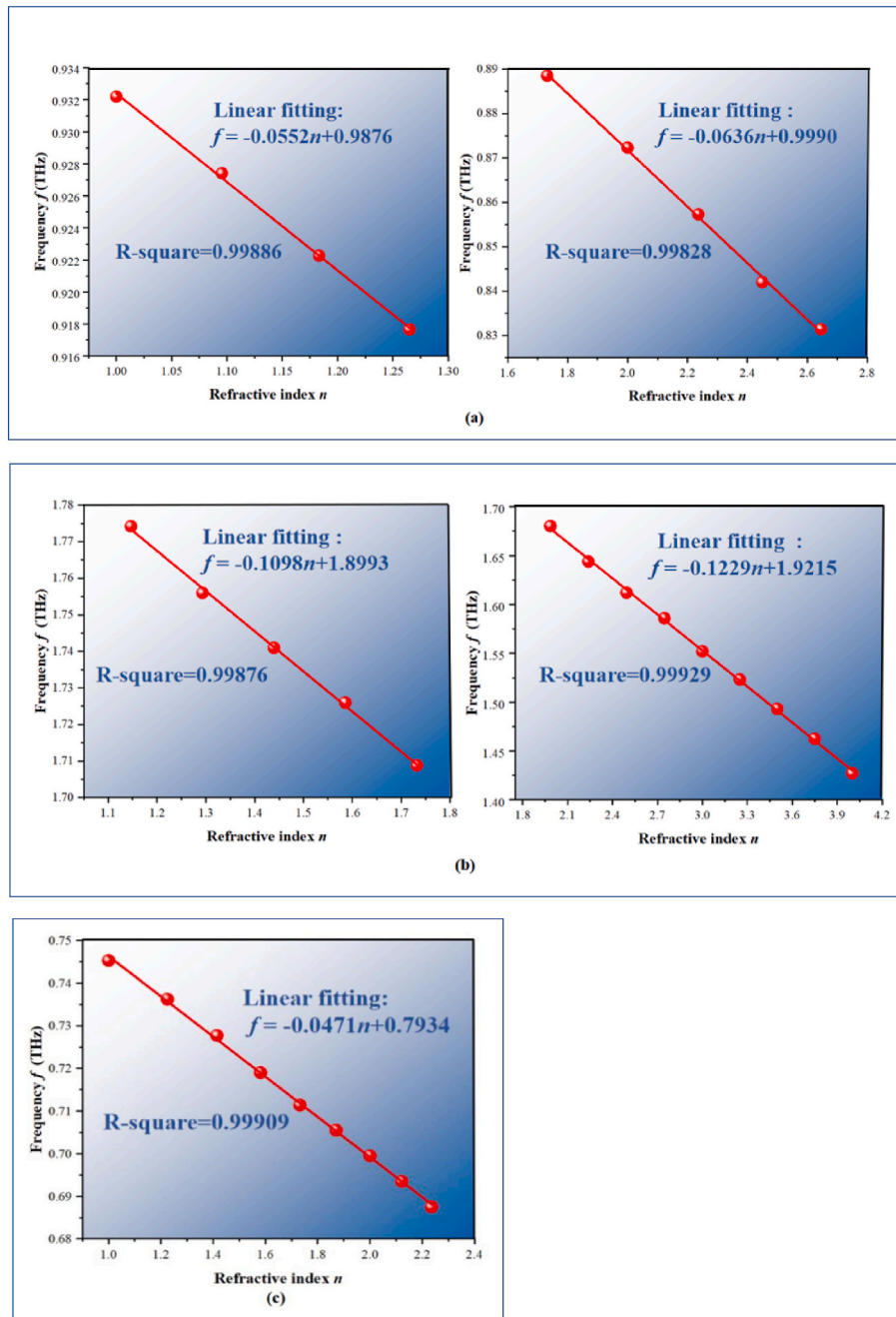
Fig. 11. The linear fitting curves in all measuring ranges. (a) Two numerical numerical measurement ranges in state 1. (b) Two numerical numerical measurement ranges in state 2. (c) The numerical numerical measurement range in state 3.

times, hence resulting in the change in absorptivity. It also deserves to be emphasized that the opposite condition occurs for the second absorption peaks of state 2 and the lower absorption point in the middle in state 3, which are slightly enhanced in Fig. 13(b) and (c) when θ is around 60°. But in brief, the absorption can keep exceeding 80% when θ is beyond 45° in all states, manifesting the stability of the MSA in the various incident angles. One of the strategies for bettering angular stability can be multiple rotations.

We also explore the absorption characteristics of the proposed structure under different polarization angles (*phi*). By virtue of the high symmetry of the MSA, the sensor is polarization-insensitive to EM waves. The variations in absorptivity when the *phi* is changed from 0° to 360° with a span of 30° are plotted in Fig. 14, where red dashed lines mark the band with absorptivity above 0.9. It can be noticed from

Fig. 14(a) that the outer optical circle is brighter than the inner one, indicating that the absorption peak at high frequency is higher, which is consistent with the previous statements. In the same way, the outermost aperture of state 2 is the brightest, thus the absorption is the best as described in Fig. 14(b). Apparently, the absorption spectra perform roughly the identical absorption effect as the *phi* increases from 0° to 360° in state 1 and state 2 except for slight varieties, proving that this structure is polarization insensitive. When we refer to state 3, the line representing 0.9 does not form a complete circle as demonstrated in Fig. 14(c), thus it can be concluded that the two absorption points at high frequency are sensitive to polarization. Overall, our proposed structure has the capability of getting rid of the sensibility of polarization.
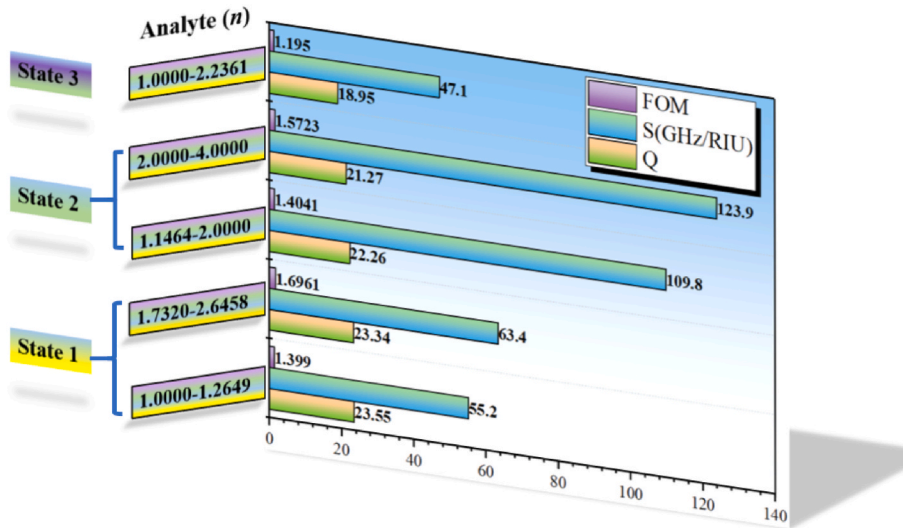
Fig. 12. Summary of FOM, S, Q in five different numerical measuring ranges for three states.

Table 2
The comparison of the optimal performance of distinct sensors.

Refs.	Measurement area	Minimum and maximum values of S	Maximum value of Q	Tunable Q	Operating states
[57]	1–1.1	3.98 μm/RIU 5.16 μm/RIU	/	Yes	one
[59]	1.59–2.4	0.513 μm/RIU 0.187 μm/RIU	/	Yes	two
[60]	1–1.2	0.452 μm/RIU	/	No	one
[61]	/	0.245 μm/RIU	/	/	two
This work	1–4	0.637 μm/RIU 0.242 μm/RIU	23.55	Yes	three

Fig. 13. (a) Absorption spectra for normally incident TE mode under different θ from 0° to 75° with a span of 15° in state 1 while $n = 1.732$. (b) Absorption spectra for normally incident TE mode under different θ from 0° to 75° with a span of 15° in state 2 while $n = 1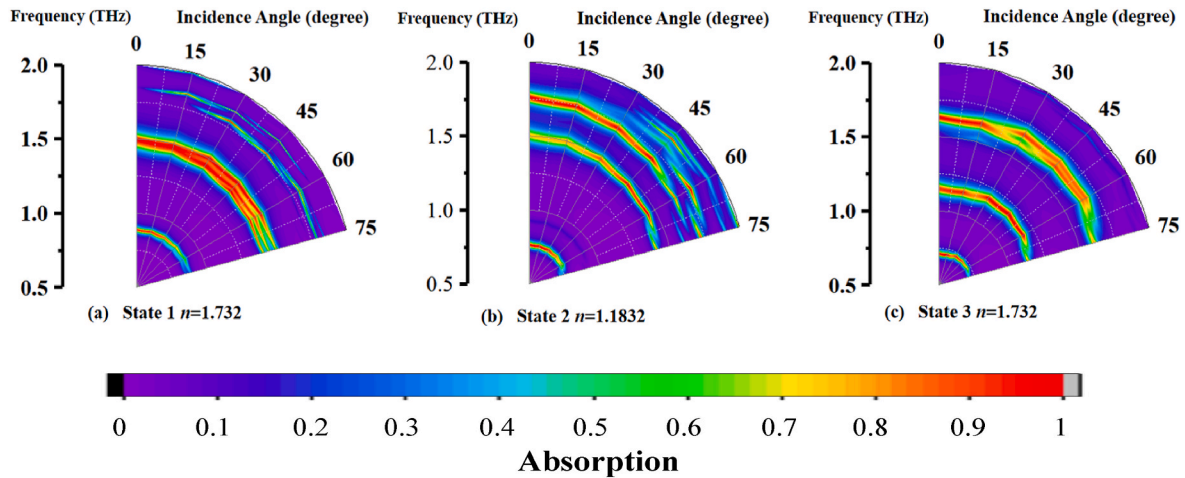.1832$. (c) Absorption spectra for normally incident TE mode under different θ from 0° to 75° with a span of 15° in state 3 while $n = 1.732$.

4. Conclusion

In conclusion, the proposed MSA, which can switch between three absorption states, is studied theoretically in various aspects. We merged two types of semiconductors Si and Ge around the metal rings. By adjusting the wavelengths of pump light, the MSA enables dynamic adjustability. Concretely, when no light pump exists, the MSA can achieve dual-band absorption at 0.9269 THz and 1.5586 THz with absorptivity of 95.32% and 99.42%; when only Ge is excited, the structure shows dual peaks absorption with absorptivity of 99.38% at 0.7790 THz

and 98.37% at 1.9506 THz; when both the Si and Ge are motivated, it can achieve dual-band absorption at 0.7490 THz with an absorptivity of 99.21% and at 1.8537 THz with an absorptivity of 99.10%.

Furthermore, the adjustable mechanism of the MSA is elucidated by the surface current distributions and electric fields at resonant frequencies in all states. The characteristics of oblique incidence and polarization angles are also analyzed and the MSA has superb tolerance of the polarization angles in three states. Additionally, the tunable MSA can serve as a sensor for refractive index sensing. It is capable of measuring five different refractive index numerical measurement ranges
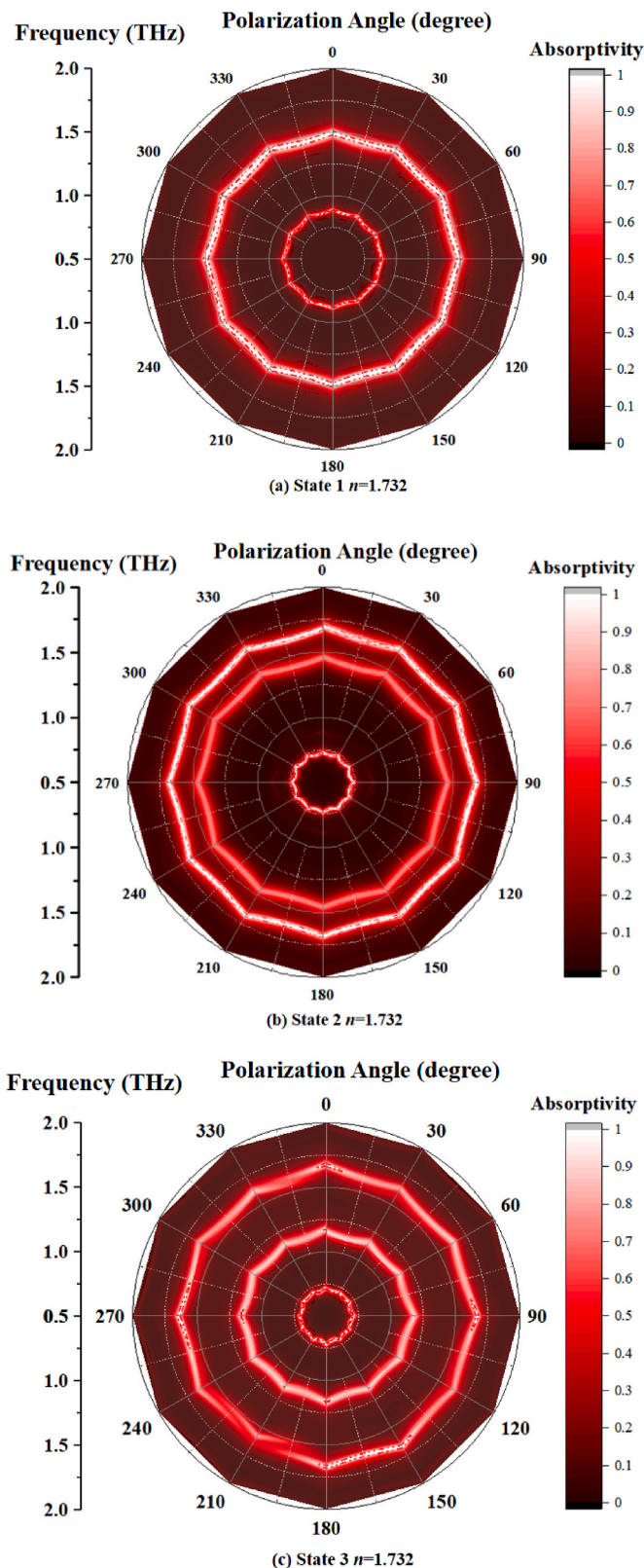
Fig. 14. The absorption spectra of the MSA varies with *phi* changing from 0° to 360° with a span of 30°. (a) state 1, $n = 1.732$. (b) state 2, $n = 1.732$. (c) state 3, $n = 1.732$.

spanning from 1 to 4 with good performance. The successful proposal of the sensor holds great promise for extensive future applications in biological detection, medical technologies, and other sensing fields.

Credit author statement

Si-Ying Li, and Hai-Feng Zhang contributed to the novel idea of the study; Si-Ying Li contributed significantly to analysis and manuscript preparation; Hai-Feng Zhang performed the data analyses and wrote the manuscript.

Declaration of competing interest

We would like to submit the manuscript entitled "An actively tunable terahertz metastructure absorber with tristate for refractive index sensing applications", which we wish to be considered for publication in this Journal. No conflict of interest exists in the submission of this manuscript, and the manuscript is approved by all authors for publication. I would like to declare on behalf of my co-authors that the work described was original research that has not been published previously, and not under consideration for publication elsewhere, in whole or in part. All the authors listed have approved the manuscript that is enclosed.

I hope this paper is suitable for this Journal. We deeply appreciate your consideration of our manuscript, and we look forward to receiving comments from the reviewers. If you have any queries, please don't hesitate to contact me.

The contact information of all authors are as following:

Hai-Feng Zhang: hanlor@163.com. Thank you and best regards. Yours sincerely, Hai-Feng Zhang Corresponding author: Name: Hai-Feng Zhang E-mail: hanlor@163.com.

Hai-Feng Zhang is the corresponding author, who is with College of Electronic and Optical Engineering & College of Flexible Electronics (Future Technology), Nanjing University of Posts and Telecommunications, Nanjing 210,023, China. (e-mail: hanlor@163.com).

Data availability

Data will be made available on request.

References

[1] Y. Fan, F. Zhang, Q. Zhao, Z. Wei, H. Li, Tunable terahertz coherent perfect absorption in a monolayer graphene, Opt. Lett. 39 (2014) 6269–6272.

[2] H. Yoshida, Y. Ogawa, Y. Kawai, S. Hayashi, A. Hayashi, C. Otani, E. Kato, F. Miyamaru, K. Kawase, Terahertz sensing method for protein detection using a thin metallic mesh, Appl. Phys. Lett. 91 (25) (2007) 253901.

[3] P.U. Jepsen, D.G. Cooke, M. Koch, Terahertz spectroscopy and imaging–Modern techniques and applications, Laser Photon. Rev. 5 (2011) 124–166.

[4] G. Yao, F. Ling, J. Yue, C. Luo, J. Ji, J. Yao, Dual-band tunable perfect metamaterial absorber in the THz range, Opt Express 24 (2016) 1518–1527.

[5] Y. Shen, T. Taday Lo, P.F. Cole, B.E. Tribe, M.C. Wr Kemp, Detection and identification of explosives using terahertz pulsed spectroscopic imaging, Appl. Phys. Lett. 86 (2005) 241116–241118.

[6] Q. Chu, Z. Song, Q.H. Liu, Omnidirectional tunable terahertz analog of electromagnetically induced transparency realized by isotropic vanadium dioxide metasurfaces, APEX 11 (2018), 082203.

[7] X. Huang, H. Yang, S. Yu, J. Wang, M. Li, Q. Ye, Triple-band polarization-insensitive wide-angle ultra-thin planar spiral metamaterial absorber, J. Appl. Phys. 113 (2013), 213516.

[8] M. Yoo, H.K. Kim, S. Lim, Electromagnetic-based ethanol chemical sensor using metamaterial absorber, Sensor. Actuator. B Chem. 222 (2016) 173–180.

[9] F. Xia, H. Wang, D. Xiao, M. Dubey, A. Ramasubramaniam, Two-dimensional material nanophotonics, Nat. Photonics 8 (2014) 899–907.

[10] S. Xiao, T. Wang, T. Liu, X. Yan, Z. Li, C. Xu, Active modulation of electromagnetically induced transparency analogue in terahertz hybrid metal-graphene metamaterials, Carbon 126 (2018) 271–278.

[11] Y. Zhang, T. Li, B. Zeng, H. Zhang, H. Lv, X. Huang, W. Zhang, A.K. Azad, A graphene based tunable terahertz sensor with double Fano resonances, Nanoscale 7 (2015) 12682–12688.

[12] R. Melik, E. Unal, N.K. Perkgoz, C. Puttlitz, H.V. Demir, Metamaterial-based wireless strain sensors, Appl. Phys. Lett. 95 (2009), 011106.

[13] Z. Li, R. Yang, J. Wang, Y. Zhao, J. Tian, W. Zhang, Multifunctional metasurface for broadband absorption, linear and circular polarization conversions, Opt. Mater. Express 11 (2021) 3507–3519.

[14] Y. Wang, R. Yang, Y. Zhao, Z. Li, W. Zhang, J. Tian, Independently tunable bifunctional terahertz metasurface based on double-layer graphene, Opt. Mater. 132 (2022), 112793.

[15] Y. Fan, R. Yang, Z. Li, Y. Zhao, J. Tian, W. Zhang, Narrowband metamaterial absorbers based on interlaced T-shaped all-dielectric resonators for sensing application, JOSA B 39 (2022) 2863–2869.

[16] N. Landy, C. Bingham, T. Tyler, N. Jokerst, D. Smith, W. Padilla, Design, theory, and measurement of a polarization-insensitive absorber for terahertz imaging, Phys. Rev. B 79 (2009), 125104.

[17] Y. Ma, Q. Chen, J. Grant, S.C. Saha, A. Khalid, D.R. Cumming, A terahertz polarization insensitive dual band metamaterial absorber, Opt. Lett. 36 (2011) 945–947.

[18] H. Zou, Y. Cheng, Design of a six-band terahertz metamaterial absorber for temperature sensing application, Opt. Mater. 88 (2019) 674–679.

[19] X. Huang, W. He, F. Yang, J. Ran, Q. Yang, S. Xie, Thermally tunable metamaterial absorber based on strontium titanate in the terahertz regime, Opt. Mater. Express 9 (2019) 1377–1385.

[20] Y. Zhao, Q. Huang, H. Cai, X. Lin, Y. Lu, A broadband and switchable VO2-based perfect absorber at the THz frequency, Opt Commun. 426 (2018) 443–449.

[21] M. Wei, Z. Song, Y. Deng, Y. Liu, Q. Chen, Large-angle mid-infrared absorption switch enabled by polarization-independent GST metasurfaces, Mater. Lett. 236 (2019) 350–353.

[22] Z. Song, M. Wei, Z. Wang, G. Cai, Y. Liu, Y. Zhou, Terahertz absorber with reconfigurable bandwidth based on isotropic vanadium dioxide metasurfaces, IEEE Photon. J. 11 (2019) 1–7.

[23] Y.T. Zhao, B. Wu, B.J. Huang, Q. Cheng, Switchable broadband terahertz absorber/reflector enabled by hybrid graphene-gold metasurface, Opt Express 25 (2017) 7161–7169.

[24] M. Huang, Y. Cheng, Z. Cheng, H. Chen, X. Mao, R. Gong, Based on graphene tunable dual-band terahertz metamaterial absorber with wide-angle, Opt Commun. 415 (2018) 194–201.

[25] R. Kowerdziej, L. Jaroszewicz, Tunable dual-band liquid crystal based near-infrared perfect metamaterial absorber with high-loss metal, Liq. Cryst. 46 (2019) 1568–1573.

[26] J.-F. Lv, C. Ding, F.-Y. Meng, J.-Q. Han, T. Jin, Q. Wu, A tunable metamaterial absorber based on liquid crystal with the compact unit cell and the wideband absorption, Liq. Cryst. 48 (2021) 1438–1447.

[27] F. Baranzadeh, N. Nozhat, High performance plasmonic nano-biosensor based on tunable ultra-narrowband perfect absorber utilizing liquid crystal, Plasmonics 16 (2021) 253–262.

[28] P. Qiao, W. Yang, C.J. Chang-Hasnain, Recent advances in high-contrast metastructures, metasurfaces, and photonic crystals, Adv. Opt Photon 10 (2018) 180–245.

[29] L. Zhang, S. Mei, K. Huang, C.W. Qiu, Advances in full control of electromagnetic waves with metasurfaces, Adv. Opt. Mater. 4 (2016) 818–833.

[30] X. Shen, T.J. Cui, Photoexcited broadband redshift switch and strength modulation of terahertz metamaterial absorber, J. Opt. 14 (2012), 114012.

[31] Y. Cheng, R. Gong, Z. Cheng, A photoexcited broadband switchable metamaterial absorber with polarization-insensitive and wide-angle absorption for terahertz waves, Opt Commun. 361 (2016) 41–46.

[32] Y. He, B. Zhang, T. He, T. Chen, G. Wang, Y. Hou, W. Xiong, J. Shen, Optically-controlled metamaterial absorber based on hybrid structure, Opt Commun. 356 (2015) 595–598.

[33] Z. Vafapour, H. Ghahraloud, Semiconductor-based far-infrared biosensor by optical control of light propagation using THz metamaterial, JOSA B 35 (2018) 1192–1199.

[37] C. Li, B. Xie, J. Chen, Z. He, Z. Chen, Y. Long, Emerging mineral-coupled composite phase change materials for thermal energy storage, Energy Convers. Manag. 183 (2019) 633–644.

[38] Z. Xiong, L. Cao, High magnetic-dielectric tunability in Ni nanocrystals embedded BaTiO3 films, J. Alloys Compd. 785 (2019) 200–205.

[39] Z. Yi, L. Liu, L. Wang, C. Cen, X. Chen, Z. Zhou, X. Ye, Y. Yi, Y. Tang, Y. Yi, Tunable dual-band perfect absorber consisting of periodic cross-cross monolayer graphene arrays, Results Phys. 13 (2019), 102217.

[40] S. Bae, H. Kim, Y. Lee, X. Xu, J.-S. Park, Y. Zheng, J. Balakrishnan, T. Lei, H. Ri Kim, Y.I. Song, Roll-to-roll production of 30-inch graphene films for transparent electrodes, Nat. Nanotechnol. 5 (2010) 574–578.

[41] S. Yuan, R. Yang, J. Tian, W. Zhang, A photoexcited switchable tristate terahertz metamaterial absorber, Int. J. RF Microw. Computer-Aided Eng. 30 (2020), e22014.

[42] S. Sze, K.K. Ng, Physics of Semiconductor Devices, A John Wiley & Sons Jnc, 2007, p. 1981.

[43] J.-S. Li, Terahertz wave modulator based on optically controllable metamaterial, Opt Laser. Technol. 43 (2011) 102–105.

[44] W. Pan, X. Yu, J. Zhang, W. Zeng, A broadband terahertz metamaterial absorber based on two circular split rings, IEEE J. Quant. Electron. 53 (2016) 1–6.

[45] Y.J. Huang, G.J. Wen, J. Li, W.R. Zhu, P. Wang, Y.H. Sun, Wide-angle and polarization-independent metamaterial absorber based on snowflake-shaped configuration, J. Electromagn. Waves Appl. 27 (2013) 552–559.

[46] J. Lee, Y.J. Yoon, S. Lim, Ultra-thin polarization independent absorber using hexagonal interdigital metamaterial, ETRI J. 34 (2012) 126–129.

[47] Y. Cheng, H. Yang, Retracted: design, simulation, and measurement of metamaterial absorber, Microw. Opt. Technol. Lett. 52 (2010) 877–880.

[48] W. Huang, W. Lin, L. Wang, L. Chang, C. Liao, Broadband optimization for a terahertz metamaterial absorber, IEEE MTT-S International Microwave Workshop Series on Millimeter Wave Wireless Technol. App. (2012) 1–3.

[49] H. Chen, O. Jf, A.K. Azad, A.J. Taylor, R.D. Averitt, D.B. Shrekenhamer, W. J. Padilla, Experimental demonstration of frequency-agile terahertz metamaterials, Nat. Immun.: Photonics (2008) 295.

[50] B.Q. Lin, J.X. Guo, B.G. Huang, L.B. Fang, P. Chu, X.W. Liu, Wideband linear-to-circular polarization conversion realized by a transmissive anisotropic metasurface, Chin. Phys. B 27 (2018), 054204.

[51] N. Shao, S.Y. Wang, W. Geyi, Circular-to-linear polarization converter based on composite via-coupled patch frequency selective surfaces, Appl. Phys. A 124 (2018) 525.

[52] H.T. Chen, J.F. O'hara, A.K. Azad, A.J. Taylor, R.D. Averitt, D.B. Shrekenhamer, W. J. Padilla, Experimental demonstration of frequency-agile terahertz metamaterials, Nat. Photonics 2 (2008) 295–298.

[53] H. Ji, B. Zhang, G. Wang, W. Wang, J. Shen, Photo-excited multi-frequency terahertz switch based on a composite metamaterial structure, Opt Commun. 412 (2018) 37–40.

[54] D.R. Smith, D.C. Vier, Th Koschny, C.M. Soukoulis, Electromagnetic parameter retrieval from inhomogeneous metamaterials, Phys. Rev. E 71 (2005), 36617–0.

[56] Q. Hong, J. Luo, C. Wen, J. Zhang, Z. Zhu, S. Qin, X. Yuan, Hybrid metal-graphene plasmonic sensor for multi-spectral sensing in both near-and mid-infrared ranges, Opt Express 27 (2019) 35914–35924.

[57] H. Shen, C. Liu, F. Liu, Y. Jin, B. Guo, Z. Wei, F. Wang, C. Tan, X. Huang, H. Meng, Multi-band plasmonic absorber based on hybrid metal-graphene metasurface for refractive index sensing application, Results Phys. 23 (2021), 104020.

[58] Z. Yi, J. Huang, C. Cen, X. Chen, Z. Zhou, Y. Tang, B. Wang, Y. Yi, J. Wang, P. Wu, Nanoribbon-ring cross perfect metamaterial graphene multi-band absorber in THz range and the sensing application, Results Phys. 14 (2019), 102367.

[59] F. Ghodsi, H. Dashti, J. Ahmadi-Shokouh, Design of a multilayer nano-antenna as a hyperbolic metamaterial with Fano response for optical sensing, Opt. Quant. Electron. 52 (2020) 1–16.

[60] G.D. Liu, X. Zhai, L.L. Wang, Q. Lin, S.X. Xia, X. Luo, C.J. Zhao, A high-performance refractive index sensor based on Fano resonance in Si split-ring metasurface, Plasmonics 13 (2018) 15–19.

[61] M.A. Otte, M.C. Estévez, L.G. Carrascosa, A.B. González-Guerrero, L.M. Lechuga, B. Sepúlveda, Improved biosensing capability with novel suspended nanodisks, J. Phys. Chem. C 115 (2011) 5344–5351.

Further reading

[34] J. Grant, Y. Ma, S. Saha, A. Khalid, D.R. Cumming, Polarization insensitive, broadband terahertz metamaterial absorber, Opt. Lett. 36 (2011) 3476–3478.

[35] Z. Song, Z. Wang, M. Wei, Broadband tunable absorber for terahertz waves based on isotropic silicon metasurfaces, Mater. Lett. 234 (2019) 138–141.

[36] S. Yuan, R. Yang, J. Xu, J. Wang, J. Tian, Photoexcited switchable single-/dual-band terahertz metamaterial absorber, Mater. Res. Express 6 (2019), 075807.

[55] X. Wang, X. Wu, J. Zhu, Z. Pang, H. Yang, Y. Qi, Theoretical investigation of a highly sensitive refractive-index sensor based on TM0 waveguide mode resonance excited in an asymmetric metal-cladding dielectric waveguide structure, Sensors 19 (2019) 1187.